FOUR-STEP SIMULATION TOOLCHAIN TO ASSESS THE EFFECTIVITY OF NOISE REDUCTION MEASURES FOR SHROUDED TAIL-ROTORS

Nicolai Stadlmair*, Daniel Redmann, Frieder Hirsch

Kopter Germany GmbH, Altlaufstr. 34, 85635 Höhenkirchen-Siegertsbrunn, Germany
nicolai.stadlmair@koptergroup.de

Victor Zappek

Technische Universität München, Lehrstuhl für Hubschraubertechnologie,
Boltzmannstr. 15, 85748 Garching, Germany

ABSTRACT

This paper presents a simulation tool-chain to study the effect of design changes on shrouded rotorcraft (tail-)rotors on its noise signature. Basically, the approach consists of four steps: The first step involves the simulation of the flow-field of the shrouded tail-rotor. The second step involves the computation of the noise far-field using the Ffowcs Williams-Hawkings (FW-H) equations in its Farassat 1A formulation. Both, step 1 and 2 are performed in the time domain. Afterwards, results are transformed to the frequency domain which improves computational efficiency and flexibility significantly. The third step is the computation of the acoustic transfer matrix to include the near-field effects of the structural elements of the tail-rotor. For this purpose, a high-fidelity finite-element model of the fluid domain surrounding the shrouded tail-rotor is introduced which is based on the frequency space formulation of the Helmholtz equations. The fourth and last step in the simulation tool chain is a terrain noise model which is based on acoustic ray tracing while results from the computed sound pressure level spheres serve as a source of ray release. The terrain noise simulation is capable to consider atmospheric attenuation as well as varying environmental and geographical conditions. In the present study, the prediction of the frequencies and relative sound pressure levels was demonstrated with acoustic measurement data acquired at a full-scale single component test-rig. The proposed toolchain uses the Kopter AW09's tail-rotor as an illustrative example to study the acoustic signature for hover and two forward-flight conditions. In this context, the spatial distribution of the noise emissions as well as the noise footprint on the ground are discussed. This serves to highlight the impact of shroud near field effects. As a practical example, the effect of a generic liner implemented upon the inner surface of the shroud is discussed. For this, directivity and noise footprint on the ground are used to benchmark the effectiveness of the liner in terms of global and local noise level reduction.

NOMENCLATURE

Symbols

A	amplitude
c	speed of sound
δ_{ij}	Kronecker Delta
E_k	turbulent kinetic energy
f	frequency
f_c	one-third octave band center frequency
h_f	flight altitude above ground
h_{mic}	microphone height above ground
I	Intensity of acoustic ray source
k	wave number
$\vec{k}$	wave vector
M	Mach number
n_i	surface normal vector
ω	angular frequency
Ω	fluid velocity potential
P	Power of acoustic ray source
p	pressure
$\vec{r}$	position vector
ϕ	phase angle
ρ	density
σ_{ij}	viscous stress tensor
TM	transfer matrix
θ	tail-rotor blade pitch angle
S	surface
t	time

Presented at 47th European Rotorcraft Forum, United Kingdom, 7-9th September, 2021

U_i	fluid velocity component in the i direction
u_n	surface normal fluid velocity
u_i	surface velocity component, i direction
v_n	surface normal velocity component
v_f	forward flight speed
x_i	location, i component
Z_S	impedance of the shroud inner surface

Indices

$[\dots]_0$	far-field
$[\dots]_{\text{source}}$	at location of sound source
$[\dots]_R$	rotor
$[\dots]_S$	shroud

1 INTRODUCTION

Since more and more light helicopters are equipped with quieter, five-blade main-rotors, such as the Kopter AW09, the contribution of tail-rotor noise gains increasingly in importance. In light of this, apart from safety and performance benefits shrouded tail rotors offer many acoustic advantages. The design of the AW09's tail-rotor already has a variety of sound-optimizing features implemented such as unevenly spaced rotor blades, dispensation of struts on the suction side of the rotor and a low tip-gap [1] between rotor blades and shroud. Conceptually, shrouded rotors still offer great potential for further passive noise reduction measures, such as the use of liners [2]. The technology is well established for the reduction of aircraft noise (see e.g. [3, 4]). For rotorcraft use, there are also studies on liner concepts [5, 6] on shrouded tail rotors.

In order to study the effectiveness of such kind of measures, accurate simulation of the noise signature of the tail-rotor is key. The most common approach to predict rotorcraft noise for a known flow field solution relies on solving the Ffowcs Williams-Hawkings (FW-H) equations in the time domain [7]. This method allows to compute the acoustic situation in the far-field originating from sound generated by a thrust-producing rotor or propeller. For open rotors, considering far-field wave propagation only is often sufficient. For encapsulated rotors, however, this simplification is harder to justify, since the direction of the sound propagation is significantly influenced by near-field effects of the shroud and even more by other structural elements such as liners. For realistic prediction of the acoustic signature of such a design also a physics based description of the noise sources and the representation of the acoustic near field of the tail-rotor is necessary. In order to assess the effectiveness of the measures, suitable modelling of the acoustic perception on the ground is also of great importance. Therefore, a methodology is needed that both computes the noise sources, accounts for the acoustic near-field and models the ground perception under realistic conditions. It is desirable to consider the underlying physics as accurately as possible while keeping the computational effort to a minimum. In addition, the chain of tools should be modular in such a way that, for example, one and the same acoustic source can be employed into different environments without requiring recalculation of the actual sources. Finally, the method shall allow to include results from component tests as well as with flight tests and/or to validate against them.

2 THEORY

In the following, the governing acoustic equations implemented in the toolchain will be briefly derived. First, the used formulation of the Ffowcs Williams-Hawkings (FW-H) equations in the time-domain will be described. Subsequently, the frequency space formulation of the acoustic wave equation, also known as the Helmholtz equation is presented. Finally, the fundamental equations describing geometrical acoustics are outlined.

2.1 Ffowcs Williams-Hawkings equations

The non-convective form of the Ffowcs Williams-Hawkings (FW-H) equations used in this study refers to Farassat's Formulation 1A and the formulation according to Dunn Farassat Padula 1A [8, 9]. In this formulation, equivalent acoustic sources are subdivided into monopole and dipole noise. The monopole term modeling the thickness noise formulated using the advanced-time formulation reads:

$$p_T(\vec{x},t) = \frac{1}{4\pi}\left(\frac{\partial}{\partial t}\int_S \left[\frac{Q}{r(1-M_r)}\right]_{\text{source}} \mathrm{d}S\right) \tag{1}$$

with

$$Q = \rho_0\left[\left(1-\frac{\rho}{\rho_0}\right)v_i + \frac{\rho}{\rho_0}u_i\right]n_i. \tag{2}$$

Loading noise is described by the dipole term:

$$p_L(\vec{x},t) = \frac{1}{4\pi}\left(-\frac{\partial}{\partial x_i}\int_S \left[\frac{L_i}{r(1-M_r)}\right]_{\text{source}} \mathrm{d}S\right) \tag{3}$$

with

$$L_i = \left[(p-p_0)\,\delta_{ij} - \sigma_{ij}\right]n_i + \rho u_i\,(u_n - v_n). \tag{4}$$

In general, similar formulations exist also for quadrupole noise, which are in principle feasible to cover with the presented toolchain. However, this type of noise source will not be considered in this study.

2.2 Helmholtz-Equations in frequency space

To solve acoustic problems with Finite Element Methods (FEM), the solution of the Helmholtz Equations formulated in frequency space is a common approach. Starting from the time domain, the equations that describe the propagation of sound in fluids can be derived from the governing equations of fluid flow. That is, conservation of mass, momentum, and energy. Additional equations of the state of the model itself and an equation of state to describe the relation between thermodynamic variables are used. The flow is assumed as lossless and adiabatic, viscous effects are neglected and a linearized isentropic equation of state is used. Under these assumptions, the acoustic field can be described by the pressure only which is governed by the wave equation, formulated in the time domain [10]:

$$\frac{1}{\rho_0 c^2}\frac{\partial^2 p}{\partial t^2} + \nabla \cdot \left(-\frac{1}{\rho_0}\nabla p\right) = 0 \tag{5}$$

Acoustic problems often involve simple harmonic waves such as sinusoidal waves which may be expanded into harmonic components via its Fourier series. Thus, the wave equation can be solved in the frequency domain for each frequency of interest. For this purpose, the harmonic solutions can be decomposed into a spatial and a temporal part using the complex formulation of the pressure variable:

$$p(\vec{x},t) = p(\vec{x}) \cdot \exp(i\omega t) \tag{6}$$

where the real part of the above mentioned equation represents the instantaneous physical value of the pressure. Using this assumption for the pressure field, the time-dependent wave equation (Eq. 5) can be expressed in the frequency space by the well-known Helmholtz equation:

$$\nabla \cdot \left(-\frac{1}{\rho_0}\nabla p\right) - \frac{\omega^2}{\rho_0 c^2} p = 0 \tag{7}$$

2.3 Geometrical acoustics

At frequencies where the wavelength is significantly smaller than the characteristic geometric dimensions the required computing power to solve Equation 7 can quickly exceed the feasibility limits. For such kind of problems, other methods like, for example, ray acoustics or energy diffusion analogies are a more suitable approach. In particular ray acoustics is applicable to model room acoustics and outdoor wave propagation over long distances. The governing equations which are solved for this purpose are briefly derived in the following.

In a stationary fluid it is often convenient to express acoustic wave propagation as a plane wave of the form by its velocity potential [11]:

$$\Omega = A \cdot \exp(i\phi) \tag{8}$$

Assuming an observer located at a distance to the source being orders of magnitude larger than the wavelength of the acoustic wave, the wave itself can be approximated as a locally plane wave, expressed by:

$$\phi = \vec{k}\vec{r} - (kct) \tag{9}$$

While the velocity potential according to Equation 8 is defined only for a fluid at rest, the same formulation can be applied to a homogeneous fluid moving at a velocity u. This is achieved by first formulating the equation of the acoustic wave in a coordinate system in which the fluid is stationary. From this, a more general form of the acoustic wave equation can be obtained:

$$\phi = \vec{k}\vec{r} - \left(kct + \vec{k} + \vec{u}\right)t \tag{10}$$

By defining the angular frequency of the wave as

$$\omega = ck + \vec{u} \cdot \vec{k} \tag{11}$$

Finally, the acoustic wave can be expressed in its Hamiltonian form:

$$\frac{\mathrm{d}\vec{k}}{\mathrm{d}t} = -\frac{\mathrm{d}\omega}{\mathrm{d}\vec{r}} \tag{12}$$

$$\frac{\mathrm{d}\vec{q}}{\mathrm{d}t} = -\frac{\mathrm{d}\omega}{\mathrm{d}\vec{k}}. \tag{13}$$

The result is a mixed time-frequency formulation, which has several advantages. On the one hand,

it allows to decompose a ray acoustics problem into its Fourier components and thus to solve its propagation for each one frequency per ray. On the other hand, it allows implementation of frequency-dependent boundary conditions in a straightforward manner.

3 SIMULATION TOOLCHAIN

In general, the proposed simulation toolchain consists of four major steps as outlined in Figure 1, which are described in the following. The first step is the conduction of a flow-field simulation with sufficient resolution in time and space to allow capturing the major physical sources of sound. In the second step, time traces of the far-field sound pressure are computed by solving the FW-H equations (Eqns. 1 and 3) in the time domain. In parallel, the acoustic transfer matrix of the structure surrounding the rotor is computed. This is achieved by solving the Helmholtz equations in frequency space using a high-fidelity FEM model of the geometry. Before applying this transfer matrix to the sound pressure levels from the FW-H computation, the time traces from the receivers are transformed to the frequency domain. Depending on the purpose of the particular analyses, one option is to extract data at the characteristic blade passing frequencies from the narrow band spectra. A second option which is used in the scope of the presented study makes use of average sound pressure levels at the one-third octave band center frequencies. In both cases the sound pressures are resolved on a spherical surface surrounding the tail-rotor geometry. In the fourth step, the sound pressure levels are imposed as a source of ray release to compute the noise footprint. Note that all steps can be considered as independent from each other. That is, the calculation of different conditions (e.g. a different sphere dimensions, surface properties of the shroud or atmospheric or terrain conditions) of each step does not imply a recomputation of the previous step. The set-up of the particular steps to obtain high quality results is described in the following.

3.1 Step 1: Computation of the flow field

To compute the main acoustic sources of a rotor or a propeller, the pressure field at the source must be known with a sufficient resolution in space and time. These sources are usually located on the surfaces of the blades, arranged at fixed, unequally distanced angles and rotating at a constant rotational speed. The option chosen in this study is to obtain the required pressure information from a transient CFD simulation of the flow-field of the shrouded rotor. In the course of this, the time resolution of the pressure fluctuations on the blade surfaces must be

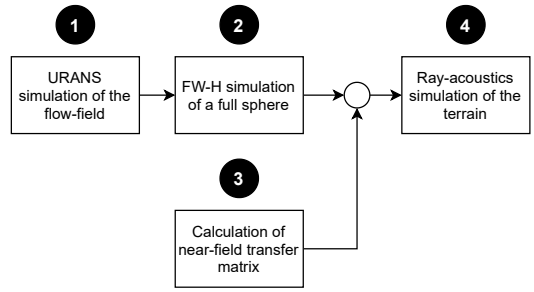

FIGURE 1: Flowchart including the four main steps of the toolchain

high enough such that the most relevant frequency range of the tail-rotor is resolved. For the given tail-rotor configuration, relevant frequencies are already known from analytical considerations and measurements and cover a range of up to approximately 3 kHz.

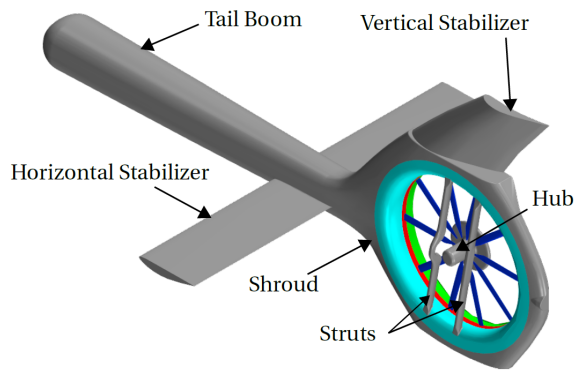

FIGURE 2: AW09 tail-boom geometry for the isolated tail-rotor study

The geometry of the used CFD set-up is shown in Figure 2. It includes the tail boom with the driveshaft fairing on top, horizontal stabilizer, vertical stabilizer, rotor hub, mounting struts of the hub, shroud itself and the ten blades of the rotor. For the tail-rotor hub a substitute geometry is used to represent its major influence on the flow-field. Note that the struts supporting the hub are located at the suction i.e. the upstream side of the rotor.

To meet the requirements of the envisaged aeroacoustic analyses, the volume mesh needs to provide a sufficient resolution of the domain. An illustration of the global mesh setup is given in Figure 3. The computational domain is a sphere with a radius that is approximately 20 times the length of the tail-boom geometry. To resolve the region of the tail-rotor blades,

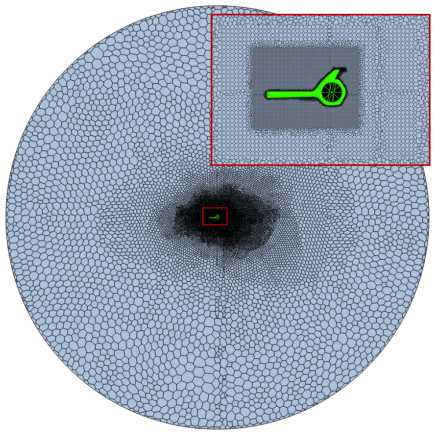

FIGURE 3: Illustration of the mesh of the entire computational domain for the tail-boom geometry

the Chimera technique is used (see Figure 4). The volume mesh consists in total of approximately 20.5 million volume cells, while more than 50% of the elements are used for the rotating blade meshes. The walls of the simulated geometry are implemented as adiabatic non-slip walls and a free-stream boundary condition is used for the far-field. The free-stream condition emulates the movement of the surrounding fluid region relative to the atmosphere.

The flow-field is computed using an implicit, unsteady time discretizing scheme for the Reynolds-Averaged Navier Stokes Equations (RANS). For turbulence modeling the $k-\omega$-SST model is used [12]. Procedurally, the first step is to achieve a converged, steady-state solution of the flow field. Subsequently, the unsteady simulation is carried out on the basis of this initial solution. From convergence studies, it has proven viable to first let the unsteady flow field

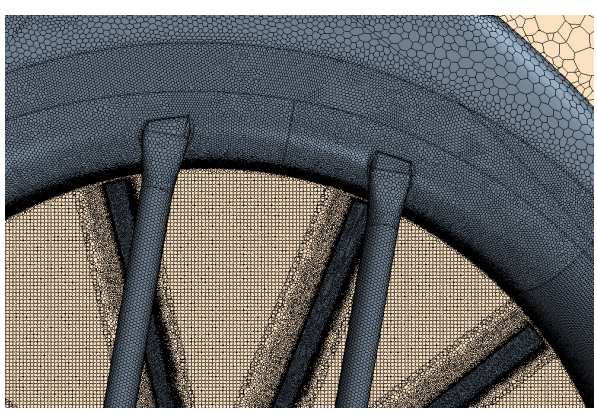

FIGURE 4: Detail view of the high-resolution mesh areas in the vicinity of the blades and the supporting struts of the tail-rotor

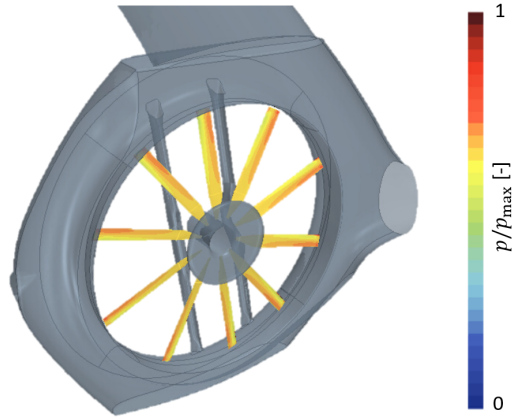

FIGURE 5: Illustration of the blade surface pressure distribution on the tail-rotor blades resulting from the unsteady flow-field simulation

settle for approx. 5 full revolutions of the rotor. Subsequently to this period, the local pressures on the blades (see Figure 5 as an illustrative example) are extracted for each time step over at least 6 additional full revolutions of the rotor. The unsteady pressure data on the blade surfaces is then transferred to the following step.

3.2 Step 2: Computation of the noise sources

As already applied in the past to other configurations of shrouded rotors [13, 14, 15, 16], the Ffowcs Williams-Hawkings (FW-H) acoustic analogy [9] is used to compute the noise sources emanating from the rotating blades. More specifically, the FW-H approach is used to calculate the sound pressures in the far-field around the tail-rotor. To provide a sufficient spatial resolution in all radiation directions a number of 344 receiver points cover a spherical surface at a fixed distance to the tail-rotor hub (see Figure 6).

The blade surfaces are assumed to be impermeable and represent the only source of sound for which monopole and dipole noise is considered. Note that calculation of quadrupole noise is also possible in principle, but has been omitted due to the focus of this paper. The FW-H solver from the commercial software package *Simcenter StarCCM+*® was used for solving Equations 1 and 3 for each time step and each receiver location subsequently to each other. Afterwards, pressures at the receiver locations are transformed to the frequency domain using a Fast Fourier Transformation (FFT). Following the analysis

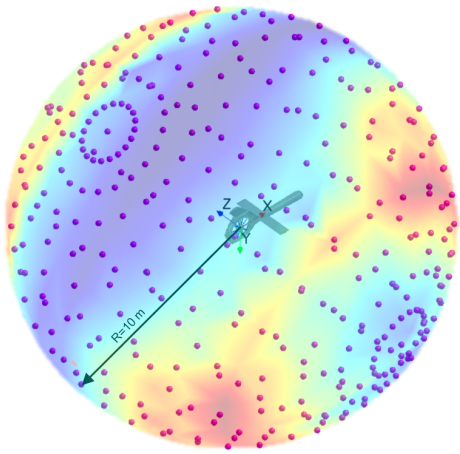

FIGURE 6: Tail-boom geometry with the spherically arranged point receivers for the FW-H computation of the far-field sound pressure

goals of this study, also one-third-octave band spectra and the Overall Sound Pressure Levels (OASPL) are calculated according to ANSI Standard S1.11-2004 [17].

3.3 Step 3: Computation of near-field effects

To capture acoustic near-field effects like reflection, refraction or absorption of incident waves, an acoustic FEM model of the tail-rotor is introduced. For this purpose, the shroud is represented as a solid body model of the 3D geometry, as depicted in Figure 7. Accordingly, the shroud geometry is incorporated into an ellipsoidal domain which is discretized into finite elements of size such that each wavelength for frequencies up to 4 kHz is covered by 4-10 tetrahedral elements. The employed discretization scheme applies quadratic Lagrangian elements. For the highest considered frequencies, the mesh consists of approximately 10 million tetrahedral cells. In addition, the acoustic far-field for which the sound pressure spectra are calculated from the FW-H simulation is represented by a sphere of the identical size. The outer surface of the ellipsoid serves as a pressure source to project the sound pressures to the sphere surface in the acoustic far-field. A linear interpolation scheme is used to match the points exactly to the receiver locations from the FW-H simulation. In the model, the ellipsoidal domain consists of dry air at a temperature of $T_\infty = 20\,°\mathrm{C}$ and a pressure of $p_\infty = 1\,\mathrm{atm}$. The used fluid model is of linear elastic type. For the ellipsoidal FEM domain, the Helmholtz equations (see Eq. 7) are solved in frequency space by a Multifrontal Massively Parallel Sparse Direct Solver (MUMPS). This method guarantees efficient and robust solution of the equation systems. The advantage here is the included out-of-core solver, which stores the lower-upper (LU) factors of the system matrix on the hard disk to minimize the internal memory requirements.

To compute the acoustic transfer matrix of the structure, the noise source of the rotor is modeled as a circular line source. Its location is set equal to 0.9 times the rotor radius. This assumption has been derived as a result from the flow-field simulation. In particular, the distribution of the turbulent kinetic energy E_k obtained in the rotor plane in the absence of a cross-flow, i.e. in the hover condition (see Figure 8) is used as an indicator for the location of the main noise source. To increase accuracy of the noise source location, the implementation of more advanced methods such as beamforming (see e.g. [18, 19]) may be used, but is not within the scope of this study. For the transfer matrix computation the source strength is fixed at a volume flow rate per unit length of $q_s = 1\,\mathrm{m^2\,s^{-1}}$. Note that this value was chosen arbitrarily, since its magnitude is eliminated by the calculation of the transfer matrix later on. All surfaces except the inner surface of the shroud are assumed as hard walls, i.e. having an infinite impedance ($Z_s = \infty$). The impedance of the inner surface is varied between $Z_s = \infty$ in the case of the base line shroud configuration and $Z_s = 0.01\rho c$ to resemble the implementation of an ideal liner. Acoustic FEM-simulations are carried out for the one-third-octave band center frequencies between $50\,\mathrm{Hz}$ and $4\,\mathrm{kHz}$. To avoid excessive computational effort, in the present study acoustic near-field properties above $4\,\mathrm{kHz}$ are assumed to be identical to the $4\,\mathrm{kHz}$ band. The acoustic transfer matrix of the shroud structure can be derived from the correlation:

$$\vec{\hat{p}}_{R,S}(f) = \mathbf{TM}_S \cdot \vec{\hat{p}}(f)_R \tag{14}$$

Where $\vec{\hat{p}}$ is the column vector of the complex valued sound pressure for each the spherically arranged FW-H receivers.The index R denotes the pressures related to the case of the rotor without shroud. The indices R,S correspond to the pressures at the same locations but including the influence of the shroud. The transfer matrix between R and R,S is denoted by $\mathbf{TM}_S$. Practically speaking, two steps are required to compute the transfer matrix: Firstly, a simulation to determine the pressure vector with ($\vec{\hat{p}}_{R,S}$) and, secondly, without shroud ($\vec{\hat{p}}_R$). Knowing these states, Equation 14 can then be solved for $\mathbf{TM}_S$, resulting in the transfer matrix between the states R and R,S, that is independent of the source strength q_s for each desired frequency. Assuming linear acoustics, the transfer matrix can also be applied to the pressures

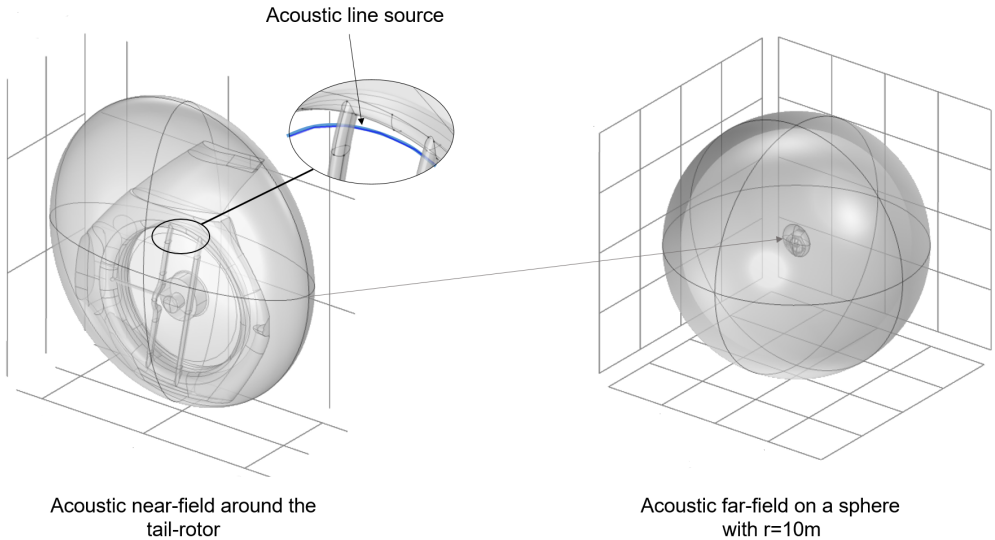

FIGURE 7: Computational domain for the acoustic FEM model of the shrouded tail-rotor

obtained from the FW-H simulation in step 3 to incorporate the influence of the shroud on the acoustic far-field. The calculation of the transfer matrix for a shroud with liner is carried out analogously, with the exception that for the state R,S a different impedance (here $Z_S = 0.01\rho c$) is imposed on the inner surface of the shroud.

3.4 Step 4: Computation of noise footprints

To compute the noise footprint on the ground, sound propagation over long distances and over a wide frequency range is considered. For this purpose, ray acoustics is used (see e.g. [20, 21]). Ray acoustics is valid for conditions where the acoustic wavelength is much smaller than the characteristic geometric features. It is thus commonly used to model e.g. room acoustics in concert halls, theaters, class rooms, or car cabins, but also for underwater acoustics, atmospheric acoustics and aircraft noise [22]. It is therefore applicable to compute the noise footprint of the tail-rotor, where frequencies between 50 and 10000 Hz are relevant and geometrical length scales in the order of magnitude of hundreds of meters are considered. The lowest considered wavelength in this model is $6.86\,\mathrm{m}$. The presented terrain noise model allows to assign boundary conditions with a variety of wall conditions, including combinations of specular and diffuse reflection. Impedance and absorption can depend on the frequency, intensity, and direction

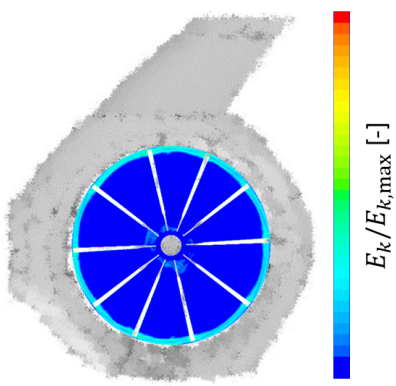

FIGURE 8: Distribution of the turbulent kinetic energy in the rotor plane extracted from the URANS flow-field simulation of the tail-rotor at $v_f = 0\,\mathrm{kts}$ (Hover)

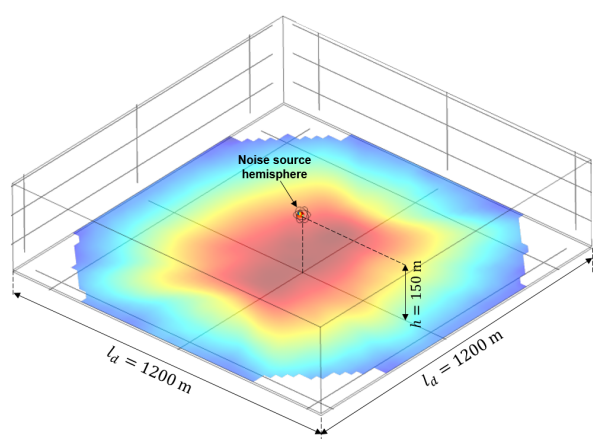

FIGURE 9: Cubical computational domain of the terrain noise model with noise footprint and source

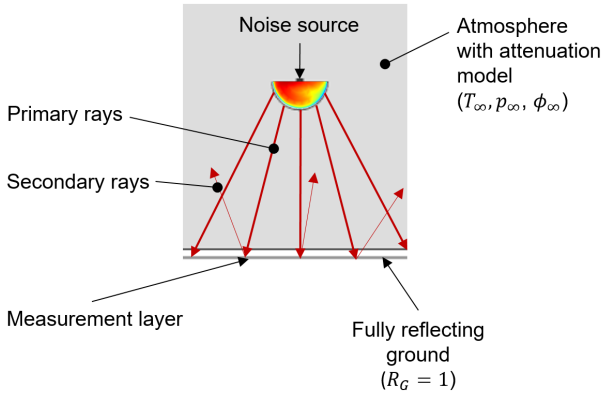

FIGURE 10: Close-up view of a sphere serving as a source of ray release in the terrain noise model

of incident rays. Transmission and reflection properties at material discontinuities can also be included. The model has also provisions to account for background velocity, for example, to model the effects of wind in atmospheric acoustics.

The used version of the terrain noise model is schematically shown in Figure 10. It basically consists of a domain with a ground surface area of 600 $\times$ 600 m. In the center of the quadratic area a sphere is located at a fixed height of $h_f = 150\,\mathrm{m}$. The surface of the sphere serves a source of ray release while its radius is identical to the radii of the sound pressure spheres known from step 2 and 3. To define the initial intensity of the ray release source, the interpolated acoustic pressures for each of the one-third octave band center frequencies f_c are prescribed in spherical coordinates according to the correlation:

$$I(r,\theta,\varphi,f_\mathrm{c}) = \frac{\hat{p}^2(r,\theta,\varphi,f_\mathrm{c})}{\rho_0 c_0} \tag{15}$$

Since in the current study only flight conditions with trajectories parallel to the ground are considered, only the ground-facing hemisphere is used. The total acoustic power emanating from this is defined as:

$$P(r,\theta,\varphi,f_\mathrm{c}) = 2\pi \cdot I(r,\theta,\varphi,f_\mathrm{c})\, r^2_\mathrm{sphere} \tag{16}$$

The propagation time for the rays is chosen such that at least a circular projection surface with a radius of 600 m on the ground is covered. Secondary rays are not of importance here, since the model does not incorporate any obstacles. For the presented setup, the propagation time is set to $T_\mathrm{ray} = 2\,\mathrm{s}$. At a speed of sound of $c = 343\,\mathrm{m/s}$ this corresponds to the time interval after which a released ray particle has travelled for a distance of 686 m. Convergence studies showed that a number of rays per release interval of N=50'000 is sufficient to obtain a smooth and gapless footprint.
In this study, atmospheric attenuation is implemented according to ANSI standard S1.26-2014 [23]. The ambient temperature for the simulations is set to $T_\infty = 20\,°\mathrm{C}$, the relative humidity is $\phi = 0.6$ and the wind speed u_∞ is set to zero. The ground is modeled as fully reflective with the impedance boundary condition set to $Z_\mathrm{ground} = \infty$. Ray release simulations are carried out for each of the one-third octave band center frequencies between 50 Hz and 10 kHz. All footprints presented below are representative for a height of $h = 1.2\,\mathrm{m}$ above the ground. Both the sphere height as well as the acquisition positions are based on the fly-over altitude above ground and microphone positions according to ICAO Annex 16 [24] Chapters 8 and 11.

4 TEST-RIG SETUP

Noise measurements from a full-scale test-rig of the AW09's tail-rotor are used to check the credibility of the computational results. The employed test-rig features the shroud and the supporting struts. The rotor is driven by an electric motor so that neither the tail-rotor gearbox nor the drive shaft are present. A schematic of the test-rig is displayed in Figure 11. For the comparison presented below, acoustic measurements from one microphone located on the downstream side of the tail-rotor are considered. Measurements were acquired with Svantek 979 sound level

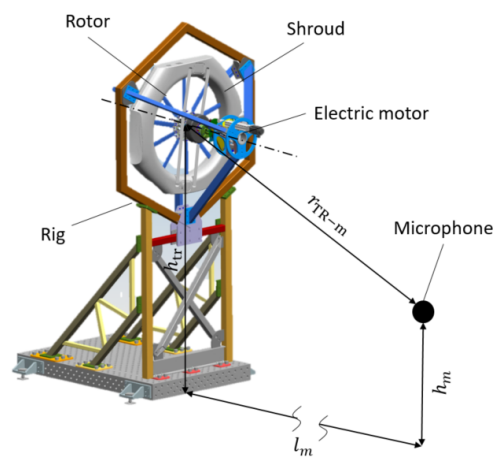

FIGURE 11: Schematic view of the full scale tail-rotor test-rig

meters at a sampling frequency of $f_s = 44\,\text{kHz}$. The devices were calibrated with a 01dB-CAL-01 acoustic calibrator (94.0 dB @ 1 kHz) before conduction of the test.
Regarding the acoustic comparability with the simulation conditions, note that the test rig is not located in an unobstructed free field, such that reflections of the sound waves are likely. Furthermore, the skid supporting the shroud as well as the electrical motor are located close to the rotor. The electric motor represents an additional noise source, from which higher measured sound pressure levels are foreseeable. From these differences, it is assumed that quantities such as absolute sound pressure levels are not directly comparable. However, important information such as frequencies and their relative amplitudes are valuable data to check the credibility of the results from the computational tool-chain.

5 RESULTS

In the following, results obtained with the presented toolchain are discussed. Within the scope of this study, three operating conditions are covered: One is the hover condition and the other two are forward-flight at a true airspeed of $v_f = 70\,\text{kts}$ and $v_f = 140\,\text{kts}$. The operating points are summarized in Table 1 which also includes the corresponding pitch angles of the tail-rotor.

For each of these operating conditions all four steps of the simulation toolchain have been run through. A breakdown of the required computational times per simulation step is given in Table 2 to get an idea of the computational effort. It can be noted that most of the computing power is allocated for calculating the unsteady flow field. For the current set-up (see Section 3.2), required computational power for the FW-H solution is about half of that demanded for the flow field solution. The required computational power for steps 3 and 4 is significantly lower than for 1 and 2. This can be attributed, among other things, to the performance advantages of the solvers working in the frequency domain. Typically, computation steps 1 and 2 need to be carried out only once for each flight case. Step 3 and 4 use the tabulated results from step 2 in the frequency domain.

TABLE 1: Operating points of the tail-rotor considered for the numerical studies

Flight case	Flight speed v_f [kts]	Blade pitch angle θ [°]
Hover	0	20
FF70kts	70	10
FF140kts	140	0

TABLE 2: Overview of computational effort for steps of the toolchain

#	Step	Computational time [CPU hours]
(1)	Flow-field solution	$\approx$ 12'000
(2)	FW-H noise sources	$\approx$ 5'800
(3)	Shroud transfer matrix	$\approx$ 260
(4)	Noise footprint	$\approx$ 6.4

In the first instance, results of the FW-H computation according to step 2 are compared to test-rig measurements. The objective of this is to show that the simulations give reasonable results in terms of frequencies and sound pressure levels. Subsequently, the impact of the near-field effects of the standard shroud and a shroud with implemented liner will be discussed for all three flight cases. In the last step, the noise footprints taken from the terrain noise simulation will be considered. From this, the influence of shroud and liner perceived on the ground are discussed.

5.1 Comparison between simulation and measurement data

This section shows the comparison of the simulation results with measurement data. For this purpose, noise measurements from the full-scale tail-rotor test-rig as described in Section 4 are used. Since the test-rig is located in a quiescent environment, simulation results belonging to the hover condition without considering near-field effects are used. Rotational speed and pitch angle at the test-rig are chosen identical to the boundary conditions of the simulation. The diagonal offset between the benchmark FW-H receiver and the microphone measurement location at the tail-rotor test-rig is less than 0.2 m. For comparison, time domain data from the FW-H simulation in hover are transferred to the frequency domain and are expressed in terms of a narrowband sound pressure level spectrum. The same procedure is used to obtain the sound pressure spectrum

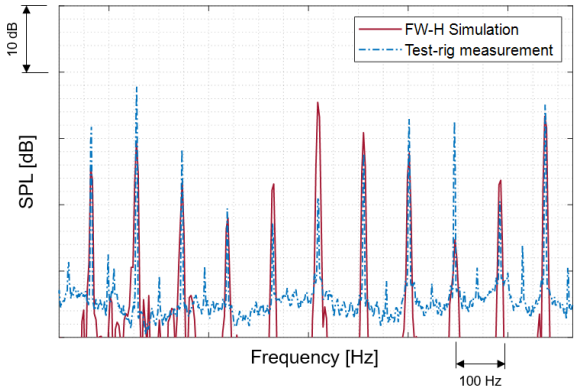

FIGURE 12: Comparison of simulated noise spectrum for a single FW-H observer with full-scale test-rig measurements

of the microphone signal. The results are shown in Figure 12. The figure indicates a very good match for the peak frequencies across the entire considered frequency range. In addition, the plot suggests that the simulation predicts the relationships between the peak heights of the blade passing frequencies (BPF) very well. In particular, the peaks corresponding to the simulation results show good agreement in terms of sharpness and prominence. For the vast majority, the levels of the measurement are above those of the simulation. Deviations can be explained primarily as a result of the different surrounding conditions between measurement and simulation. That is, on the one hand, reflexions and scattering of the sound wave are likely to occur. One the other hand, the test site accommodates power-controlled supply equipment such as a power generator and an electric motor to drive the rotor of the test-rig, which are not eliminated by background sound measurements. Therefore, higher noise levels than in the simulation are to be expected.

5.2 Direct noise emissions of the tail-rotor

The spatial distribution of the noise signature of the shrouded tail-rotor will be discussed in the following. Results are presented on the basis of spheres enclosing the tail-rotor with the contour illustrating the overall sound pressure levels (OASPL). As a representative example, the hover flight-case is selected. The main objective of this analysis is to point out the differences in the noise signature between the FW-H calculations after step 2 and the incorporation of the near-field effect of the shroud after step 3, respectively. The third case considered is the shroud with liner. It is important to note that the prediction of the liner effect is only feasible when taking into account the shroud geometry imposed with the respective surface impedances at the desired locations. Figure 13 depicts the contours of the OASPL on the sphere surface of the tail-rotor for the hover case for the direct FW-H calculation (a) as well as including reflection and diffraction effects for the standard shroud (b) and the case including an ideal liner (c). Comparing case (a) and (b) highlights a notable influence of the shroud structure on the noise signature in the far-field. By including the transfer matrices, the sound pressure levels emerge as less homogeneous and increasingly concentrated in narrow regions. These regions show in general higher peak amplitudes and sharper gradients across the sphere surface. This effect can be explained by the imposed location of the main source and the guidance effect of the sound-hard shroud dictated by the transfer matrix $\mathbf{TM}_S$. As a comparison, Figure 13(c) represents the noise signature after the transfer matrix $\mathbf{TM}_{S,L}$ was applied. Note that this implies that the inner surface of the shroud perpendicular to the rotor axis contains a lining surface with a constant, real-valued surface impedance of $Z_S = 0.01\rho c$. It can be seen that the noise signature with liner mainly shows a reduction in the level rather than a global deflection of the sound waves compared to the changes between (b) and (a). This seems plausible since the impedance was imposed on the entire surface and does not depend on the frequency. Note that an ideal liner has been assumed which has a real-valued surface impedance. A more significant change in the radiation pattern would be visible if only certain sections were impeded. This can be relevant, for example, if liners are only implemented in certain segments due to design constraints. Design studies for the selective guidance of directivity would also be possible.

5.3 Noise signature on the ground

Finally, footprints of the tail-rotor's noise signature computed by the terrain noise model are analyzed. The results are representative for an unobstructed environment at a flight altitude of $h = 150\,\mathrm{m}$ above ground. The displayed sound pressure levels correspond to a height of $h_m = 1.2\,\mathrm{m}$ above the ground. The highlighted circle has a diameter of $r = 150\,\mathrm{m}$ for which line-plots will be discussed afterwards. The nose of the helicopter resp. the flight direction always points in the positive x-direction. All results shown here include the near-field impact of the tail-rotor shroud geometry. To give a first indication of the global sound emission behavior, the OASPL will be used. As for the sphere plots, the OASPL footprints result from computations using the one-third-octave bands between 50 Hz and 10 kHz for all three flight cases (v_f =[0, 70, 140] kts) without ($Z_S = \infty$) and with ideal liner ($Z_S = 0.01\rho c$).

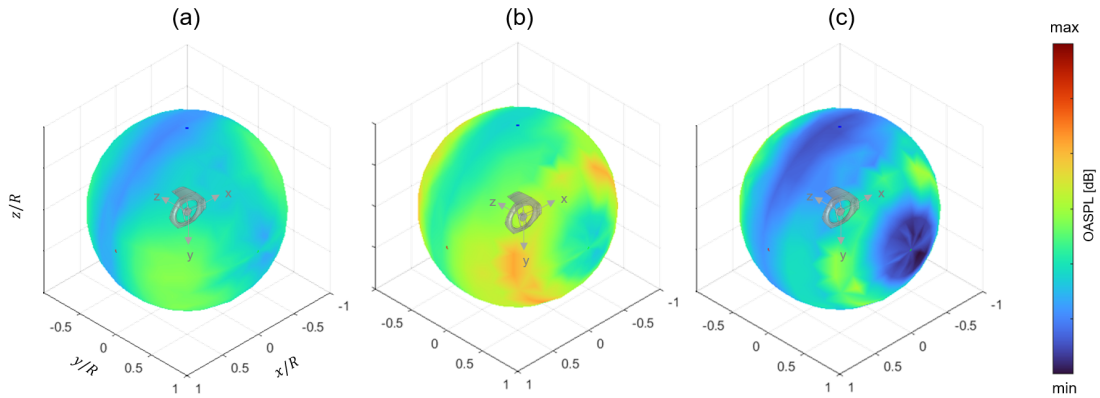

FIGURE 13: Spheres with contours representing the OASPL for the hover condition for (a) FW-H calculation and including the near-field effects of the shroud (b) and with ideal liner with impedance of 0.01 ρc (c)

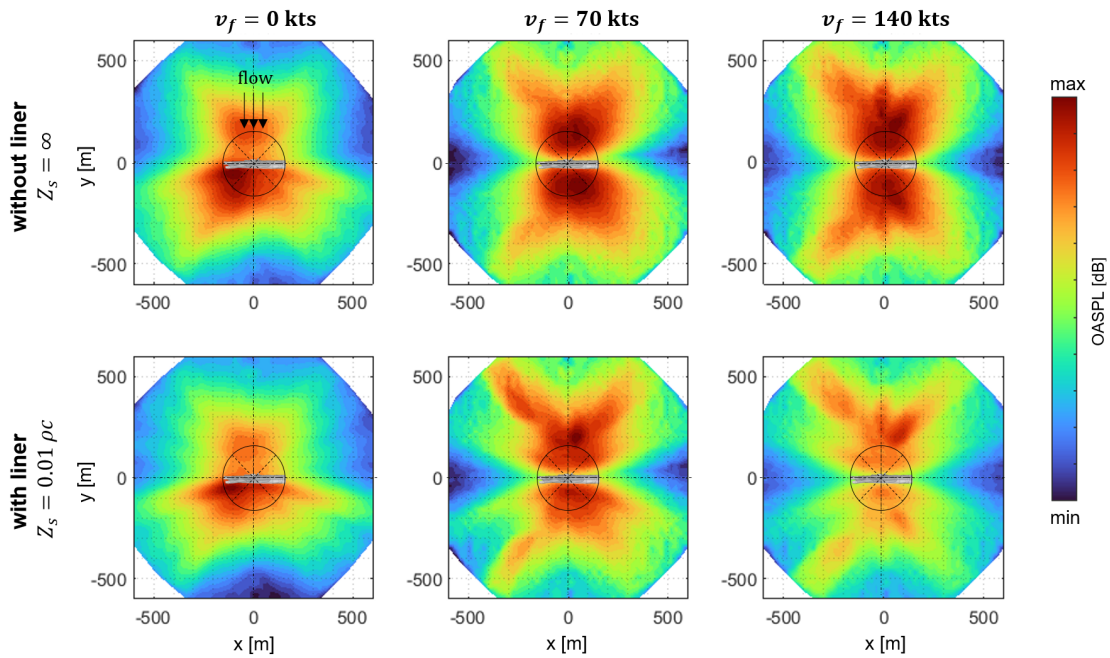

FIGURE 14: Noise footprints at a height of $h_{\text{mic}} = 1.2\,\text{m}$ above the ground, at a flight altitude of $h_f = 150\,\text{m}$ above the ground for hover ($v_f = 0\,\text{kts}$) and two flight speeds comparing with and without liner implemented in the tail-rotor shroud

Figure 14 shows the footprints on a plane surface with the extent of 1200 x 1200 m. Note that for $v_F > 0$ the footprint moves with the helicopter trajectory in the positive x-direction. From the figures clear distinctions in the footprint between hover and forward-flight become evident. For hover, the OASPL contours indicate a significantly lower average total sound pressure level on the ground than in forward flight. The levels on the suction side ($y > 0$) are noticeably lower than on the pressure side ($y < 0$). The areas characterized by high sound pressure levels appear in the quadrant near the aft position starboard. Looking at both forward flight cases, the noise contours reveal only minor differences between the suction and pressure side of the tail-rotor. One explanation for this is the distribution of acoustic energy between flight states with and without forward velocity. As can be derived from the narrowband noise spectra (not shown here), the acoustic emissions in the hover case are clearly dominated by BPF noise. This results from the large thrust produced by the high blade pitch angles and the absence of a cross flow velocity. In forward flight the low blade pitch angle and high influence of a cross flow due to high flight speed in-

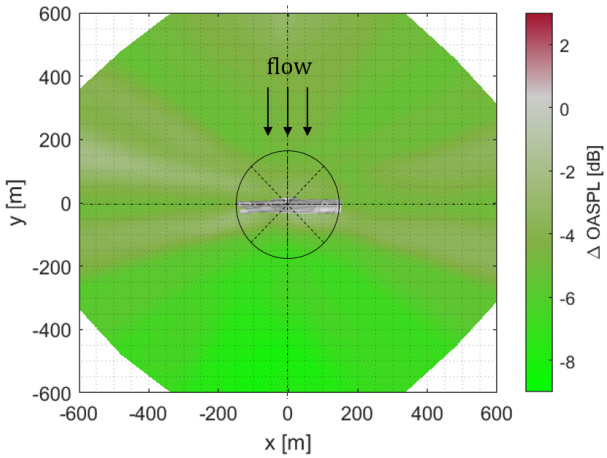

FIGURE 15: Noise footprints at a height of $h_{\text{mic}} = 1.2\,\text{m}$ above ground, at a flight altitude of $h_f = 150\,\text{m}$ above ground for hover ($v_f = 0\,\text{kts}$) and 2 flight speeds with and without liner implemented in the tail-rotor shroud

creases the influence of broadband noise. This contributes to a sound signature with less directional dependence in forward flight. At first sight, the case with liner ($Z_S = 0.01\rho c$) indicates a marked reduction of the average OASPL across all three considered flight conditions. In the scope of this study, the efficiency of the liner is governed by the imposed real-valued surface impedance causing the absorption of sound energy. At a second glance, however, the footprints also reveal local distinctions when a liner is implemented. These local differences can be seen more clearly in Figure 15. The figure displays the differential footprint in terms of OASPL for the hover case with and without the liner. Besides the global reduction of the overall sound pressure levels also local differences emerge. The highest reduction effect between 6 and $9\,\text{dB}$ can be observed in a conical area on the pressure side at a distance of about $100\,\text{m}$ from the center of the rotor. The reduction effect in the closer vicinity ($-100\,\text{m} < y < 100\,\text{m}$) of the rotor is significantly lower (approx. 2 to 4 dB). Beyond that the reduction potential is also predicted to be lower on the suction side.

From the results, it can be clearly seen that the effect of a lining surface inside the shrouded (tail-) rotor can be used not only to reduce the levels but moreover to guide the noise emissions in a targeted direction. Potentially, this computational method can support the development of a liner design to optimize sound radiation for one or more flight altitudes within a certain radius around the aircraft. As an illustrative example, Figure 16 highlights the noise reduction potential in hover on a defined circle of $r = 150\,\text{m}$. Note that the OASPL only reflects global noise emissions. From an engineering point of view, a differentiated consideration of individual frequency ranges in particular at the characteristic blade passing frequencies is of interest. While these options are considered in the tool chain, it is not the subject of this study.

A further important aspect of noise reduction measures on a rotorcraft is the impact on the noise certification value. Depending on the applicable regulations, which in turn depend on the weight class of the helicopter, different flight conditions and measurement positions are of interest. One case that is relevant to certification according to ICAO Annex 16 [24], Chapter 8 and 11 is the straight-line overflight at an altitude of $h = 150\,\text{m}$ at 90% of the maximum achievable flight speed. The closest conditions within the scope of the present study is the forward flight at $v_F = 140\,\text{kts}$. The objective of the following analysis is to obtain a first impression of the impact of the liner at locations relevant for certification. For this purpose, Figure 17 shows the time evolution of the OASPL in dB measured at lateral distances of $\pm 150\,\text{m}$ and without lateral offset ($y = 0$) to the flightpath. For noise certification according to ICAO Annex 16 [24] Chapter 11 only the latter position is of relevance while for Chapter 8 all three positions are mandatory. In the figure, the configurations without

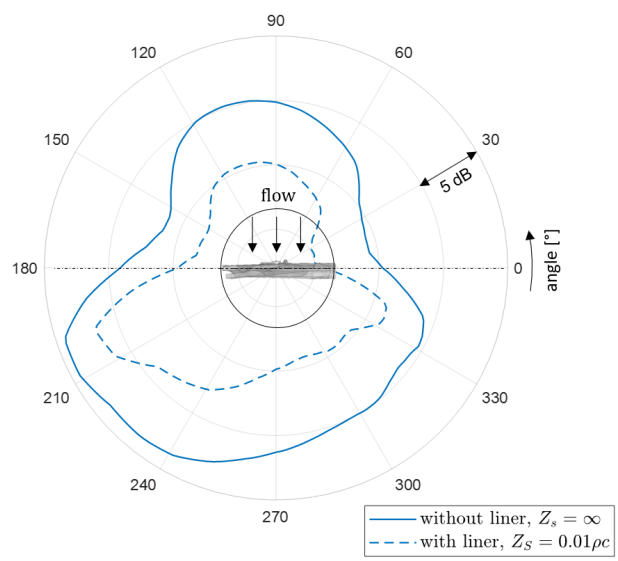

FIGURE 16: Overall sound pressure levels on a circle with a radius of $r = 150\,\text{m}$ at a height of $h_{\text{mic}} = 1.2\,\text{m}$ above the ground, at a flight altitude of $h_f = 150\,\text{m}$ above the ground for hover ($v_f = 0\,\text{kts}$) comparing the case with and without liner implemented in the tail-rotor shroud

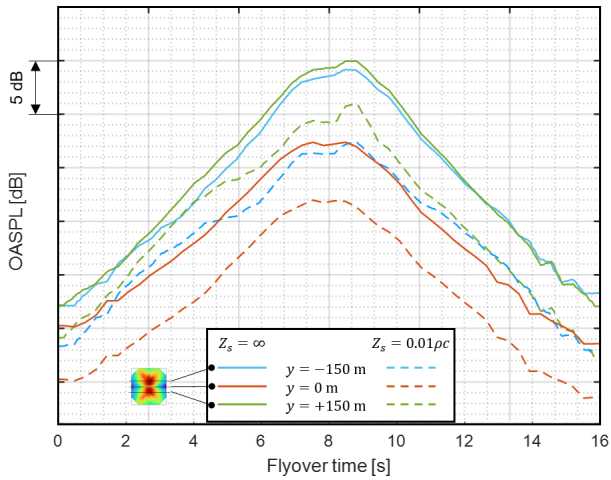

FIGURE 17: Fly-over flight paths for noise certification according to ICAO Annex 16, Chapter 8 and 11 [24] for forward flight at a flight speed of $v_f = 140\,\text{kts}$ with and without ideal liner

($Z_S = \infty$) and with liner ($Z_S = 0.01\rho c$) are compared. It can be seen that the largest effect of the investigated liner configuration is predicted for the microphone position located directly below the flight path (on average $\Delta\text{OASPL} \approx 5.2\,\text{dB}$). On the starboard side ($y = -150\,\text{m}$) the OASPL is reduced by $\approx 4.9\,\text{dB}$ while a noticeably lower reduction is computed for the port side located ($y = 150\,\text{m}$) microphone. Here the average reduction is found to be $\Delta\text{OASPL} \approx 3.8\,\text{dB}$. Note that the evaluation of certification metrics such as SELdB and EPNLdB has been avoided here by intention. Since for conventional helicopters the main rotor is considered to be the main source of sound, it affects the 10dB-downtime substantially. Thus the main rotor must always be included when the quantitative influence of noise reduction measures at secondary sources on the certification levels is of interest. The presented terrain noise model allows to consider of multiple sources, provided that their spatial characteristics are available e.g. in the form of a spherical description. However, since the main focus of this study is the introduction of a comprehensive simulation tool-chain for a shrouded tail-rotor, the main rotor is not considered here.

6 CONCLUSIONS AND OUTLOOK

In the present paper a comprehensive and computationally efficient toolchain for the simulation of passive noise reduction measures for shrouded (tail-)rotors was introduced. The toolchain consists of four major computational steps, namely (1) flow-field simulation using URANS, (2) computation of the acoustic sources using the FW-H approach, (3) consideration of the near field acoustics with acoustic FEM and (4) evaluation of noise footprints with a terrain noise model. Prediction of the frequencies and relative sound pressure levels was demonstrated with acoustic measurement data acquired at a full-scale component test-rig. The necessity to account for the near-field acoustics of the shroud using step (3) was highlighted by discussing spheres and noise footprints with and without including the acoustic transfer matrix of the shrouded tail-rotor. Based on this, a study on the effect of a generic, ideal liner implemented upon the inner surface of the shroud was shown. In the course of this, directivity and the noise footprint on the ground were discussed. As a concluding remark, a simulation method was presented that offers the potential to perform detailed design studies for passive damping measures such as liners. Due to its modularity, the method provides a high level of computational efficiency, since the acoustic sources need to be computed only once, while design studies in the frequency domain can be performed with short computational times.

The next stage of development of the toolchain envisages consideration of the main rotor as well as other noise sources such as the engine(s). This shall pave the way towards a compuationally efficient, fully physics based prediction of the helicopter's noise signature. An important industrial use case of this method is to anticipate the impact of design changes on helicopter noise certification values already in early design stages. Due to the use of the ray acoustics method the terrain noise model offers the possibility to consider environmental conditions such as buildings, different of ground or geographical conditions like mountains. Also varying ambient conditions such as humidity, wind or atmospheric layers can be implemented. It is planned to extend the simulation step (4) in order to model real ambient conditions for a better exploitation of flight test data during imperfect measurement conditions. In addition, extensions towards low-noise approach and take-off procedures are planned e.g. for heliports or vertiports for eVTOLs.

paper, for the publication and distribution of this paper and recorded presentations as part of the ERF proceedings or as individual offprints from the proceedings and for inclusion in a freely accessible web-based repository.

REFERENCES

[1] Ewald, D., Pavlovic, A., and Bollinger, J. G., 1971. "Noise reduction by applying modulation principles". *Journal of the Acoustical Society of America,* ***49***(5A), pp. 1381–1385.

[2] Longhouse, R. E., 1978. "Control of tip-vortex noise of axial flow fans by rotating shrouds". *Journal of sound and vibration,* ***58***(2), pp. 201–214.

[3] Parrott, T. L., and Watson, W. R., 2005. "Status of Duct Liner Technology for Application to Aircraft Engine Nacelles". In NOISE-CON 2005.

[4] Ma, X., and Su, Z., 2020. "Development of acoustic liner in aero engine: a review". *Science China Technological Sciences*, pp. 1–14.

[5] Pongratz, R., and Redmann, D., 2016. "Acoustic Liner Design for Fenestron Noise Reduction". In 42nd European Rotocraft Forum.

[6] Schneider, S., Heger, R., and Konstanzer, P., 2017. "BLUECOPTER™ demonstrator: The state-of-the-art in low noise design". *73rd AHS International Annual Forum*(09/2016), pp. 1–3.

[7] Ffowcs Williams, J. E., and Hawkings, D. L., 1969. "Sound generation by turbulence and surfaces in arbitrary motion". *Philosophical Transactions of the Royal Society of London. Series A, Mathematical and Physical Sciences,* ***264***(1151), pp. 321–342.

[8] Ffowcs-Williams, J. E., 1996. "Aeroacoustics". *Journal of Sound and Vibration,* ***190***(3), pp. 387–398.

[9] Farassat, F., 2007. "Derivation of Formulations 1 and 1A of Farassat". *NASA Technical Memorandum*(NASA/TM-2007-214853).

[10] Pierce, A. D., and Beyer, R. T., 1990. Acoustics: An introduction to its physical principles and applications. 1989 Edition.

[11] Landau, L. D., and Lifshitz, E. M., 2013. *Course of theoretical physics*. Elsevier.

[12] Menter, F., 1993. "Zonal two equation kw turbulence models for aerodynamic flows". In 23rd Fluid dynamics, plasma dynamics, and lasers conference, p. 2906.

[13] Falissard, F., Desmerger, F., Gardarein, P., Binet, L., and Camus, J. C., 2011. "Aeroacoustic flight test data analysis for the validation of Fenestron noise computations". In Proceedings of the American Helicopter Society 67th Annual Forum. Virginia Beach.

[14] You, J., Thouault, N., Breitsamter, C., and Adams, N., 2012. "Aeroacoustic analysis of a helicopter configuration with ducted tail rotor". *28th Congress of the International Council of the Aeronautical Sciences 2012, ICAS 2012,* ***2***, pp. 1–13.

[15] Kowarsch, U., Ohrle, C., Keßler, M., and Krämer, E., 2015. "Aeroacoustic simulation of a complete H145 helicopter in descent flight". In 41st European Rotorcraft Forum.

[16] You, J. H., Breitsamter, C., and Heger, R., 2016. "Numerical investigations of Fenestron™ noise characteristics using a hybrid method". *CEAS Aeronautical Journal,* ***7***, pp. 182–207.

[17] American National Standards Institute, 2004. *ANSI S1.11-2004: Specification for Octave-Band and Fractional-Octave-Band Analog and Digital Filters*.

[18] Dougherty, R. P., 2008. Noise source imaging by beamforming. Tech. Rep. 0518, SAE Technical Paper.

[19] Horváth, C., Envia, E., and Podboy, G. G., 2014. "Limitations of phased array beamforming in open rotor noise source imaging". *AIAA Journal,* ***52***(8), pp. 1810–1817.

[20] Pierce, A. D., 2019. *Ray Acoustics*. Springer International Publishing, Cham, pp. 427–486.

[21] Attenborough, K., and Van Renterghem, T., 2021. *Predicting outdoor sound*. CRC Press.

[22] Brouwer, H. H., 2014. "A ray acoustics model for the propagation of aircraft noise through the atmosphere". *International Journal of Aeroacoustics,* ***13***(5-6), pp. 363–383.

[23] American National Standards Institute, 2014. *ANSI/ASA S.126-2014: Methods for Calculation of the Absorption of Sound by the Atmosphere*.

[24] International Civil Aviation Organization (ICAO), 2017. *Annex 16 - Environmental Protection - Volume I - Aircraft Noise*.